THE ASTROPHYSICAL JOURNAL, 413:304–316, 1993 August 10

NEAR- AND MID-INFRARED IMAGING OF THE PLANETARY NEBULAE BD +30°3639 AND IC 418

JOSEPH L. HORA
Institute for Astronomy, 2680 Woodlawn Drive, Honolulu, HI 96822-1839
LYNNE K. DEUTSCH
U. C. Berkeley; and NASA/Ames Research Center, NASA/Ames Research Center, M/S 245-6, Moffett Field, CA 94035
WILLIAM F. HOFFMANN
Steward Observatory, 949 North Cherry Avenue, Tucson, AZ 85721-0655
GIOVANNI G. FAZIO
Harvard/Smithsonian Center for Astrophysics, MS 65, 60 Garden Street, Cambridge, MA 02138
AND
KANDIAH SHIVANANDAN
General Research Corporation, 1215 Jefferson Davis Highway, Suite 900, Arlington, VA 22202
Received 1992 October 7; accepted 1993 February 18

ABSTRACT

We present near- and mid-infrared images of the planetary nebulae BD +30°3639 and IC 418 with a unique combination of high spatial and spectral resolution. The mid-infrared images were obtained with MIRAC, a new IR array camera. For BD +30°3639, the mid-IR images at 10.0, 11.2, 12.4, 12.8, and 13.2 μm have allowed us to separate the various spectral emission components such as the broad UIR features (perhaps from large molecular grains), the 12.8 μm [Ne II] emission feature, and continuum emission to determine the distribution of these components in the nebula. The derived temperature and opacity images show the detailed distribution of temperature and relative density of the dust. For IC 418, we have obtained high-resolution images in both the near- and mid-infrared. The images in the near-infrared at J, H, and K are important for determining the source of the IR excess; we have determined that one component of the excess is located near the central star and is possibly due to nonequilibrium heating of small grains. We have also imaged the halo emission at H and K, which has been detected in earlier studies, and have determined its spatial extent. The mid-IR images at 9.8 and 11.7 μm show continuum emission coincident with the ionized zone and suggest that silicon carbide emission originates from the region near the central star.

Subject headings: dust, extinction — planetary nebulae: individual (BD +30°3639, IC 418)

1. INTRODUCTION

In the final stages of stellar evolution, many evolved stars eject and ionize their outer envelopes to form planetary nebulae (PNs). The processed material in these ejected envelopes is returned to the interstellar medium (ISM) and subsequently incorporated into new stars. Thus the PN stage bears important consequences for the evolution of the ISM and stellar populations. Yet the composition, interaction, and processing of the grain and gas populations in PNs and the mechanisms responsible for the ejection and observed morphologies of these circumstellar envelopes are not well known. Most PNs exhibit an "infrared excess" and distinct morphologies at infrared (IR) wavelengths of continuum and spectral feature emission which can help to identify the differences in composition and physical environment of the emitting material. Near- and mid-IR imaging provides the high spatial and spectral resolution required to study the form and content of PNs.

In the near-IR, there are several components which may contribute to the total observed flux from a PN. These include nebular emission from recombination and collisionally excited lines, hydrogen bound-free continuum emission, molecular hydrogen emission, and a continuum component from hot dust. Also, there is usually a significant emission component from the central star of the PN. At mid-IR wavelengths, possible components are a warm ($\approx$200 K) dust continuum and emission lines due to Ne, Ar, and S. A broad feature attributed to SiC grains near 11.3 μm and a silicate feature near 9.7 μm may also be present. Many IR-bright nebulae exhibit several unidentified infrared (UIR) emission features in the near- and mid-IR. The UIR features are observed in a wide variety of astronomical sources. It has been suggested that these features are emitted by one or more of a group of small molecules called polycyclic aromatic hydrocarbons (PAHs; Léger & Puget 1984).

Large-aperture spectrophotometry blends the observed flux from spatially distinct emission zones. The presence of spectral feature emission in spatially confined regions can be masked if the feature intensity is small compared to the integrated continuum emission over a large aperture in the feature wavelength. High spatial resolution imaging can reveal the presence of spectral features which may not be detected in large aperture measurements and will identify different populations of emitters in the circumstellar envelope. Spatial differences in the emission at continuum and spectral feature wavelengths of dust and gas and the location of the emission with respect to the central star distinguish the physical conditions within the nebula which heat, excite, and destroy the emitters.

In this paper, we present near- and mid-IR images of the PNs BD +30°3639 and IC 418 with a unique combination of

high spatial and spectral resolution. The mid-IR images of BD +30°3639 have allowed us to separate the various spectral components such as the broad UIR emission features, the 12.8 μm [Ne II] emission feature, and continuum emission to determine the distribution of these components in the nebula. The derived temperature and opacity images show the detailed distribution of temperature and relative density of the dust. For IC 418, we have obtained high-resolution images in both the near- and mid-IR. The images in the near-IR are important for determining the source of the IR excess; we have determined that one component of the excess is located near the central star and is possibly due to non-equilibrium heating of small grains. We have also imaged the halo emission, which has been detected in earlier studies, and have determined its spatial extent.

2. OBSERVATIONS AND DATA REDUCTION

All of the observations at *J*, *H*, and *K* presented here were obtained with the 64 × 64 Hg:Cd:Te array camera (Rieke, Rieke, & Montgomery 1987) on the Steward Observatory (SO) 2.3 m telescope at Kitt Peak. The general observing procedure was to take pairs of images consisting of an exposure of the source, followed by an exposure of the same duration at a telescope offset of 60″ off the source. Standard star images were obtained before and after observations of the PN for the flux calibration. Also, images were obtained of SAO catalog stars near the PN to measure the point spread function (PSF) of the system at the time of the PN observations. The SAO star would be typically a few arcmin from the PN, so this provided a good measurement of the PSF for that time and part of the sky.

To reduce the data, the successive on- and off-source images were differenced to remove the background signal. The resulting image was multiplied by a gain matrix to remove pixel variations in gain. Typically 32–64 images were obtained at each filter, at 20–60 s per image, depending on the magnitude. The images were aligned and averaged to produce the final image. For all of the PNs presented here, the sizes of the nebulae were smaller than the field of view of the array, so each on-source frame contained an image of the entire nebula.

The mid-IR images presented here were obtained with Mid-IR Array Camera (MIRAC) on the SO 2.3 m and 1.5 m telescopes. The MIRAC system and data taking procedure are described in detail elsewhere (Hora 1991; Hoffmann et al. 1993). The camera uses a Hughes Aircraft Co. 20 × 64 arsenic-doped silicon "impurity band condition" (IBC) hybrid array with a capacitive transimpedance amplifier (CTIA) readout. The array is sensitive to IR radiation from 2 to 26 μm. Reflective optics provide scales of 0.″66 pixel^{-1} and 0.″34 pixel^{-1} on the SO 2.3 m telescope. The camera dewar contains two cold filter wheels with 10% spectral resolution filters at 8.8, 9.8, 11.7, amd 12.5, μm, an 8% filter at 20.2 μm, a circular variable filter (CVF) with 1.8% resolution from 7.9 to 14.5 μm, 8% filter at 20.2 μm, a circular variable filter (CVF) with 1.8% resolution from 7.9 to 14.5 μm, standard near-IR filters *K*, *L*, and *M*, and several neutral density filters. The NEFD of MIRAC on the SO 2.3 m telescope at 11.7 and 12.5 μm was measured during the course of these observations to be 7 mJy arcsec^{-2} in 15 minutes of on-source integration, 1 hr total time. The 5 σ sensitivity for a point source spread over 9 pixels (3.9 arcsec^2) is 70 mJy.

Images of BD +30°3639 were obtained at 10.0, 11.2, 12.4, 12,8, and 13.2 μm using the CVF. The image of IC 418 at 11.7 μm was taken using the discrete filter at that wavelength with a bandpass of 1.13 μm. Gain matrices were calculated from blank sky images taken at 1 and 2 airmasses. When observing the sources, a combination of chopping the secondary and "wobbling" or "nodding" the telescope was used. The source was in only one of the four chop-nod beams. The chopper throw was approximately 25″ toward the north, at a frequency of 5 Hz, and the nod beam position used was 30″ W of the first position. Many images were taken at each wavelength, with an offset of a few arcseconds between each. The images were then registered to the nearest 0.25 pixel and averaged to produce the final image.

3. BD +30°3639

The PN BD +30°3639 is an optically bright, round, highly symmetric low-excitation nebula (see the images in Balick 1987). Radio continuum images (Basart & Daub 1987; Masson 1989) have shown that the structure is double-lobed, with peaks at the north and south positions of a nebular ring. The IR emission from BD +30°3639 has been studied extensively. Early observations showed the nebula to have excess IR emission (Woolf 1969). Russell, Soifer, & Merrill (1977) observed the UIR features around 3.3 μm in their near-IR spectrum. Moseley (1980) observed far-IR continuum emission, along with a strong feature near 30 μm. Aitken & Roche (1982) obtained an 8–13 μm showing UIR and [Ne II] emission features, which were confirmed in the *IRAS* measurements of BD +30°3639 (Pottasch et al. 1986). Results of near-IR imaging of BD +30°3639 by Roche (1989) and Smith et al. (1989) have been reported, and mid-IR imaging studies of BD +30°3639 have been carried out by Bentley et al. (1984), Hora et al. (1990), and Ball et al. (1991).

3.1. *BD +30°3639 Observations*

The details of the BD +30°3639 observations are given in Table 1, along with the measured flux at each wavelength. The total time listed is on-source integration time in seconds. The resolution given is the measured FWHM of the profile of the SAO star used for the PSF determination at that wavelength. The IR standard star HD 203856 was used for flux calibration at *K* (Elias et al. 1982). The PSF standard for the *K* image was a field star in the same frames as the nebula. The flux standards used for the mid-IR images were τ Dra and β Peg. Images at each of the six wavelengths are shown in Figure 1.

3.2. *BD +30°3639 2.2 Micron Image*

The observed 2.2 μm flux from BD +30°3639 contains contributions from recombination emission, continuum emission from hot dust, and emission from the central star. To obtain a measure of the flux from the nebula alone, the contribution from the central star must be subtracted out. The result of subtracting the scaled PSF reference star image is shown in Figure 2. The image is slightly irregular in the central part of the nebula due to a slight alignment mismatch between the images, but overall the central star is subtracted properly to reveal the nebular structure. The total flux of the subtracted central star was 0.084 Jy, giving a total flux for the nebula alone of 0.448 Jy.

The image of BD +30°3639 in Figure 2 shows the nebular emission to be ring-shaped, with two bright lobes in the northern and southern portions of the ring. The northern lobe is

TABLE 1

OBSERVATION LOG

Date (UT)	Telescope and Instrument[a]	Wavelength (μm)	On-Source Time (s)	Flux (Jy)	Resolution
		BD +30°3639			
1989 Dec 14	1	2.2 (*K*)	400	0.532	1".3
1991 Jun 3	2	10.0	540	51	1.5
1991 Jun 3	2	11.2	400	96	1.5
1991 Jun 2	2	12.4	220	89	1.7
1991 Jun 2	2	12.8	240	138	1.7
1991 Jun 3	2	13.2	420	88	1.6
		IC 418			
1990 Mar 6.....	1	1.2 (*J*)	560	0.82	1.32
1989 Dec 13	1	1.6 (*H*)	320	0.73	1.56
1989 Dec 14	1	2.2 (*K*)	680	1.24	1.18
1991 Nov 21	2	9.8	200	34	1.6
1990 Dec 6	3	11.7	60	29	2.5

[a] (1) = SO 2.3 telescope, Hg:Cd:Te array camera, 0".58 pixel^{-1}; (2) = SO 2.3 m telescope, MIRAC, 0".66 pixel^{-1}; (3) = SO 1.5 m telescope, MIRAC, 1".0 pixel^{-1}.

slightly brighter. This is very similar to the spatial distribution of emission seen in radio continuum images of this nebula (Basart & Daub 1987; Masson 1989). The images match very closely, with the only significant difference being an extension of the northern lobe to the east. As described below, there is also an enhancement of the mid-IR emission in this location in several of the images, which points to an origin in dust emission.

3.3. *BD +30°32639 Mid-IR Images*

Mid-IR images of the PN BD +30°3639 have been published previously, by Bentley et al. (1984) using a single element detector; by Hora et al. (1990) using the AMCID camera; and by Ball et al. (1991) using the Berkeley/IGPP mid-IR camera. Our previous observations using the AMCID camera (Hora et al. 1990) were obtained at the IRTF with lower spatial resolution than the images presented here due to charge spreading effects in the detector array. The spectral resolution of the current observations is also higher, using the 2% bandwidth CVF instead of individual 10% filters, so the feature images will contain less continuum flux and will more accurately show the spatial distribution of the feature emission. The wavelengths of the current observations were chosen to sample the UIR feature at 11.2 μm, the [Ne II] line at 12.8 μm, the UIR emission "plateau" at 12.4 μm, and continuum wavelengths near these features. With the two mid-IR continuum images at 10.0 and 13.2 μm, we can better estimate the continuum level at the feature wavelengths in order to subtract the continuum flux contribution, and a color temperature image can be calculated (§ 3.3.3). Finally, the 12.8 μm image is an important addition since the [Ne II] feature traces the distribution of the ionized gas, which can now be directly compared to the dust continuum and features at the same spatial resolution and under the same observing conditions.

One issue discussed in previous studies is the spatial distribution of the spectral features in the nebula relative to the continuum emission. This is important for models of the formation and destruction of dust and the identification of the feature carriers. The carriers of the UIR emission may be destroyed within the ionized zone. Bentley et al. and Hora et al. find that the UIR emission in BD +30°3639 is slightly more extended than the continuum emission by a small amount. Ball et al., however, report finding no difference in the spatial extent of the UIR or [Ne II] feature emission compared to the continuum emission.

3.3.1. *Comparison of Continuum and Feature Emission Spatial Distribution*

To address the issue of the relative spatial distribution of continuum and feature emission, we compare the images presented here in two ways, using two-color images in continuum and feature wavelengths, and source profiles. The color images of BD +30°3639 are shown in Figure 3 (Plate 18). The emission at continuum and feature wavelengths is compared in each two-color image by displaying the 10.0 μm continuum image in green and the other wavelength in red. Where the relative brightness is similar, the image appears yellow; otherwise in the either red or green depending on which image is relatively brighter at that position. Along much of the nebula in the 10.0–11.2 μm comparison (Fig. 3*a*), the outer edge is red and the inner edge is green. The 11.2 μm emission is spatially more extended in these regions, especially in the N and E parts of the nebula. In the 10.0–12.4 μm image (Fig. 3b), the spatial extent is less defined, with green and red regions showing up near both the inner and outer edge. The 10.0–12.8 μm comparison image (Fig. 3*c*) shows that the 12.8 μm [Ne II] emission is greatest in the N and S regions of the nebula, whereas the continuum dust is relatively brighter in the E and W regions. In the comparison between the continuum images at 10.0 and 13.2 μm (Fig. 3*d*), there are green and red sections on the nebular ring, indicating warmer or cooler dust emission regions.

Both the 11.2 and 12.4 μm images contain UIR emission ("feature" and "plateau," respectively), but the color images in Figure 3 show that their spatial distribution is different. In most UIR-emitting sources, the 11.2 μm feature and the plateau emission are almost always observed together (e.g., Witteborn et al. 1989). Yet in BD +30°3639, the emission seems to be produced in different regions of the nebula. This

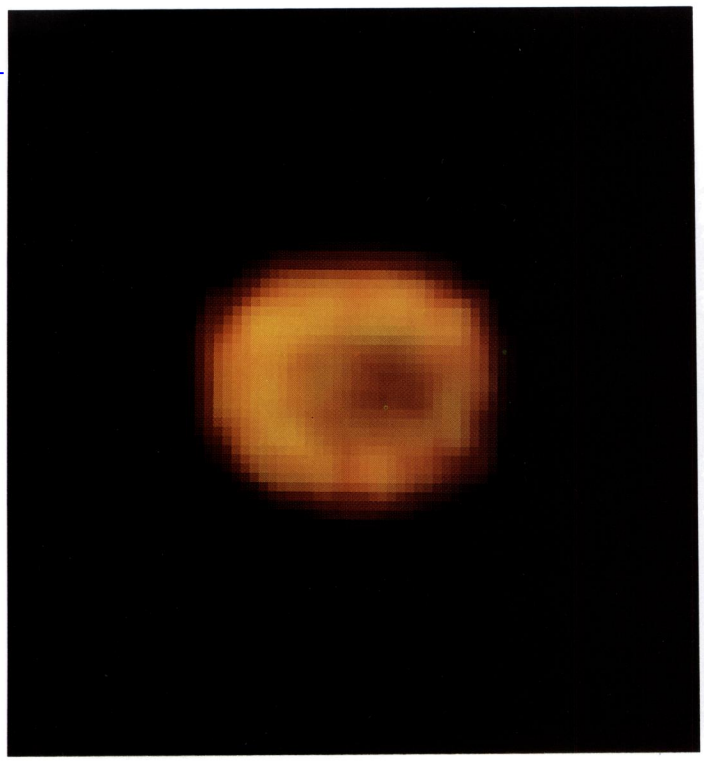

FIG. 3*a*

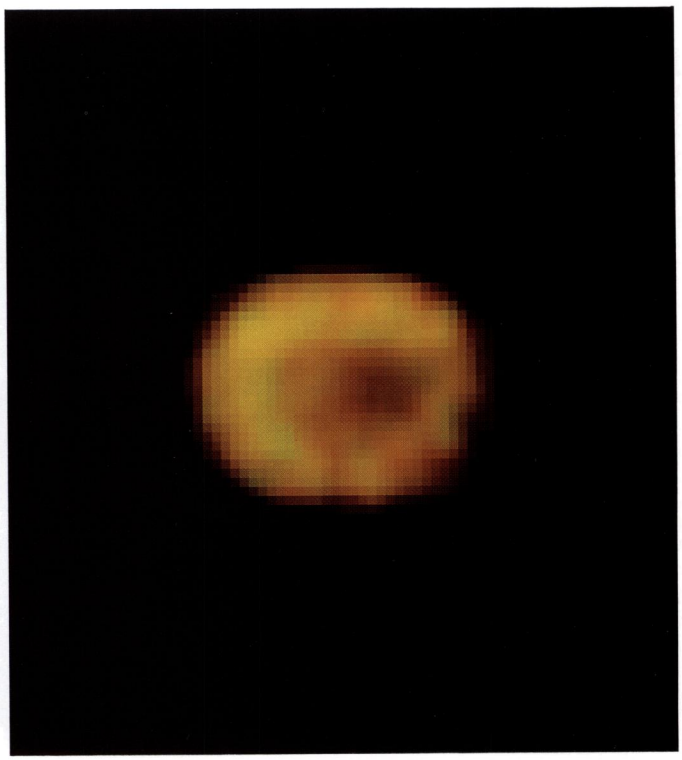

FIG. 3*b*

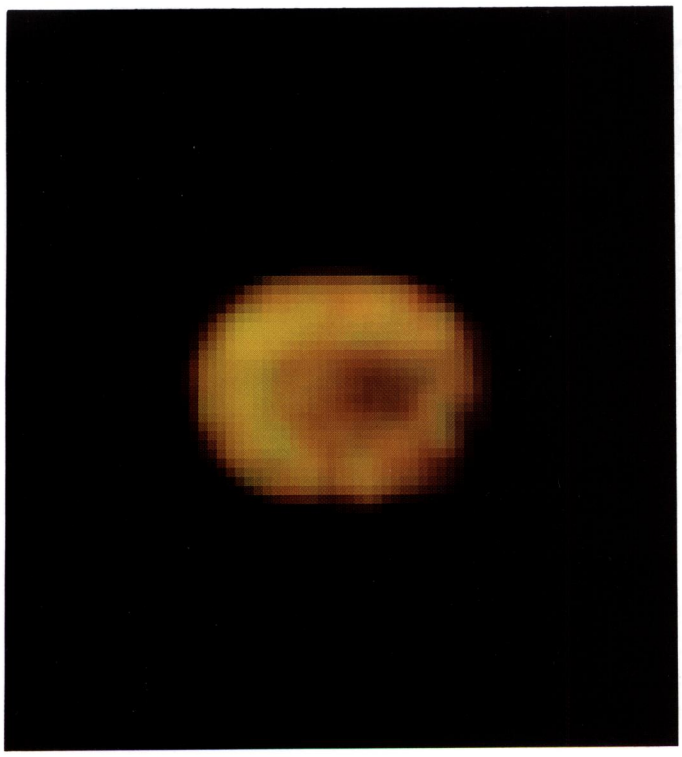

FIG. 3*c*

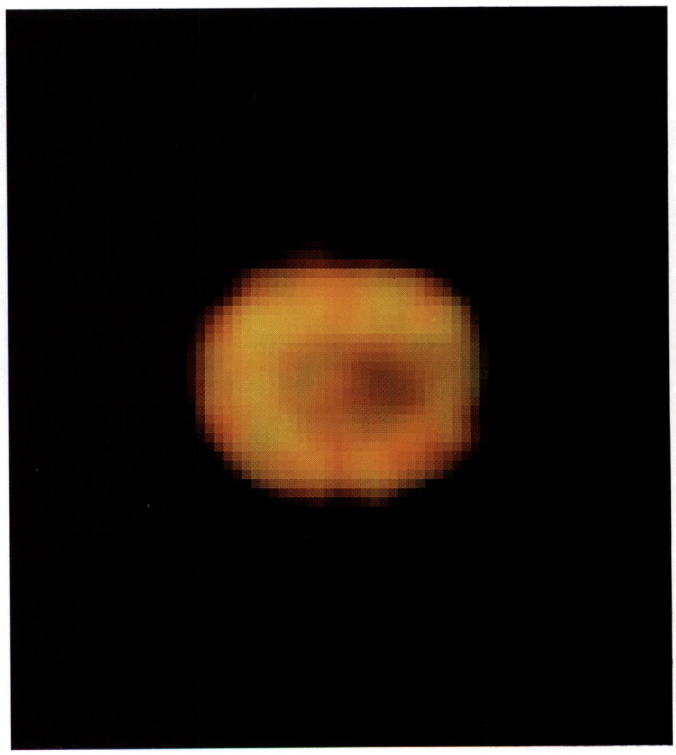

FIG. 3*d*

FIG. 3.—False-color images of BD +30°3639 showing differences in the spatial distribution of the emission. In each of the images, the 10.0 μm image is assigned green, and the other wavelength is assigned red. (*a*) 10.0 μm, 11.2 μm image. (*b*) 10.0 μm, 12.4 μm image. (*c*) 10.0 μm, 12.8 μm image. (*d*) 10.0 μm, 13.2 μm image.

HORA et al. (see 413, 306)

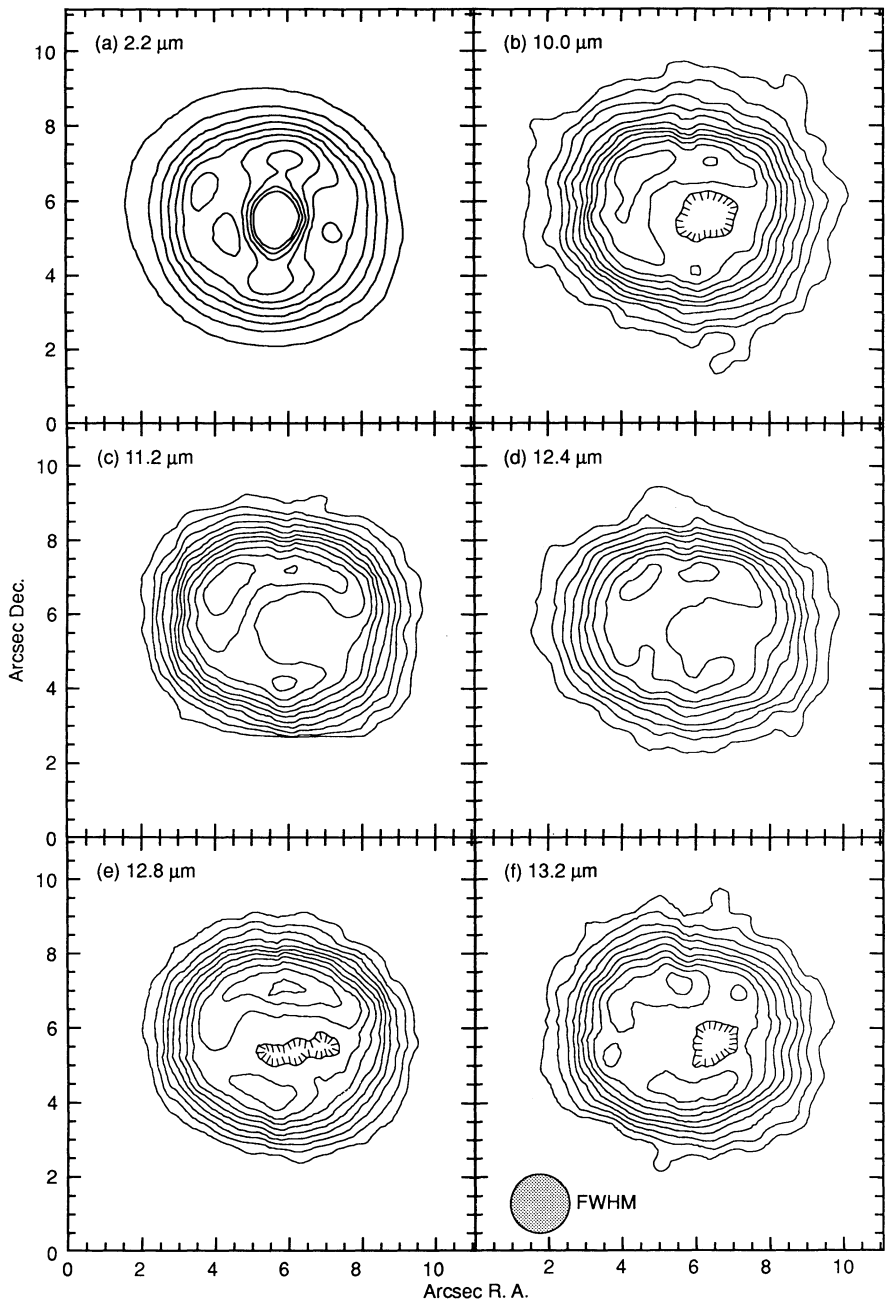

FIG. 1.—Contour images of the planetary nebula BD +30°3639. The contour level spacings in the mid-IR maps were chosen to be spaced evenly between a minimum and the maximum value of the map. In all cases the minimum contour level is $>5\sigma$ above the background noise level. The circle in the 13.2 μm panel (*f*) is the FWHM size of the standard star image at that wavelength (1".6), typical for the mid-IR images (see Table 1). (*a*) 2.2 μm: contour spacing 2.5 mJy arcsec^{-2}, minimum level 2.5 mJy arcsec^{-2}. (*b*) 10.0 μm: contour spacing 150 mJy arcsec^{-2}, minimum level 200 mJy arcsec^{-2}. (*c*) 11.2 μm: contour spacing 200 mJy arcsec^{-2}, minimum level 500 mJy arcsec^{-2}. (*d*) 12.4 μm: contour spacing 250 mJy arcsec^{-2}, minimum level 450 mJy arcsec^{-2}. (*e*) 12.8 μm: contour spacing 400 mJy arcsec^{-2}, minimum level 900 mJy arcsec^{-2}. (*f*) 13.2 μm: contour spacing 300 mJy arcsec^{-2}, minimum level 600 mJy arcsec^{-2}.

indicates that these may be different mechanisms for producing the two different types of emission, or that the excitation of the feature and plateau emission depend differently on the conditions in various positions in the PNs such as temperature, density, or radiation field.

There is a significant continuum component to the flux in the 11.2 and 12.8 μm images. Figure 2 shows [Ne II] feature and 11.2 μm UIR feature images in which the continuum has been subtracted. The continuum level in each image was estimated by scaling the nearest continuum image (10.0 and 13.2 μm for the 11.2 and 12.8 μm images, respectively) assuming a blackbody temperature structure given by the temperature image in Figure 2 (see § 3.3.3). Figure 4 shows profiles through these two images, with the profile of the 10.0 μm continuum image included for comparison. The UIR profiles are more extended than the continuum in both profiles, in FWHM size and distance between the peaks. The FWHM sizes and separations between the profile peaks are listed in Table 2. The

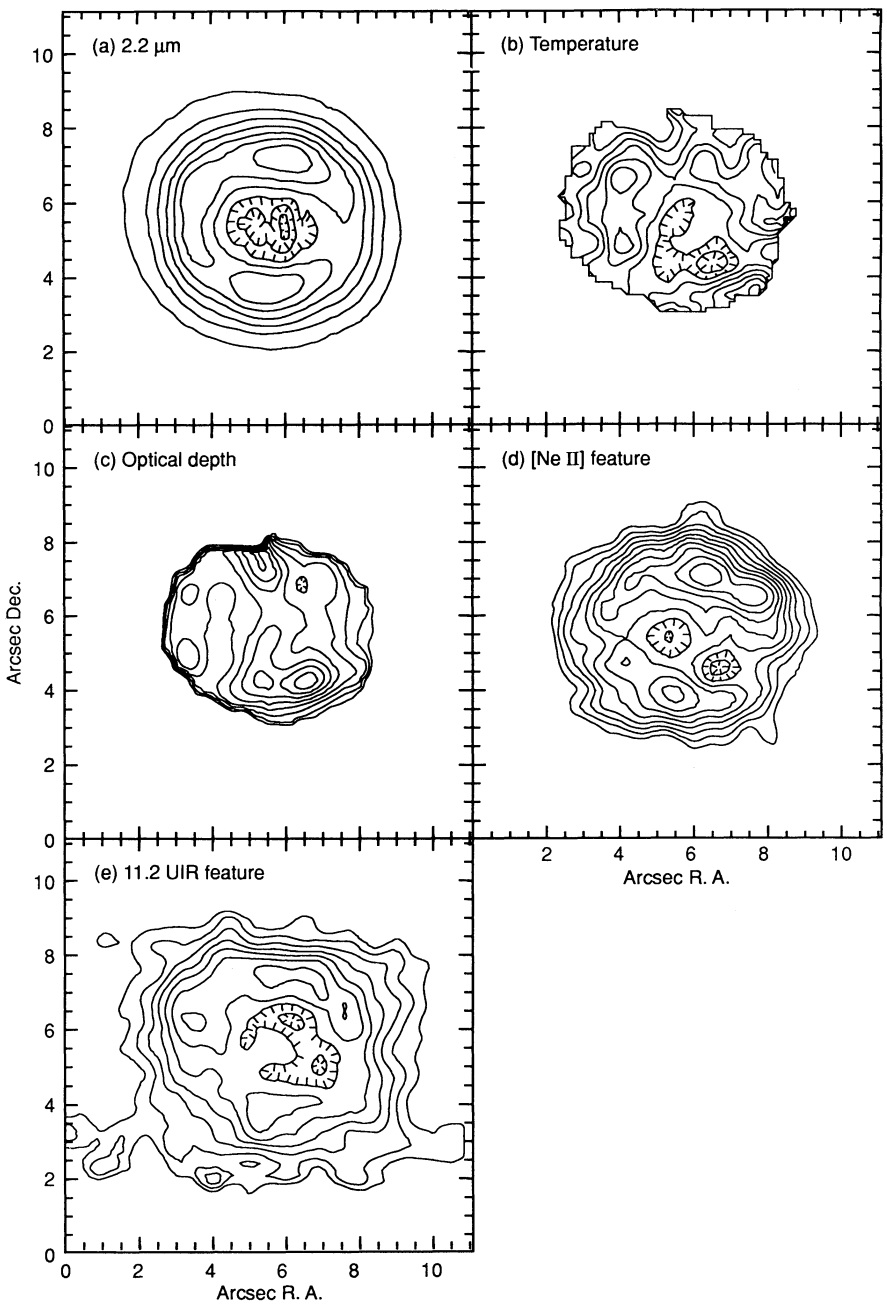

FIG. 2.—Images of BD +30°3639 derived from the data images in Fig. 1. (*a*) Contour image of BD +30°3639 at 2.2 μm, where the central star contribution has been subtracted, showing the nebula alone. Contour levels are evenly spaced at 2.5 mJy arcsec^{-2}, with a minimum level of 2.5 mJy arcsec^{-2}. (*b*) Temperature image of BD +30°3639, calculated from the 10.0 and 13.2 μm images. Contour levels are evenly spaced at 4 K per level, with a minimum level of 160 K. (*c*) Dust opacity image of BD +30°3639, calculated from the temperature image of Fig. 2*b* and the 10.0 μm intensity image. Contour levels are evenly spaced at 1×10^{-3}, with a minimum value of 3×10^{-3}. (*d*) Contour image of the 12.8 μm feature of BD +30°3639, calculated from the 12.8 μm image and a scaled 13.2 μm image from Fig. 1. The contour level spacing is 150 mJy arcsec^{-2}, with a minimum level of 300 mJy arcsec^{-2}. (*e*) Contour image of the 11.2 μm feature of BD +30°3639, calculated from the 11.2 μm image and a scaled 10.0 μm image from Fig. 1. The contour level spacing is 100 mJy arcsec^{-2}, with a minimum level of 100 mJy arcsec^{-2}.

[Ne II] image is close to the same size as the continuum in the S-N profile (FWHM is similar, although the peaks have a larger separation), but is larger in the E-W profile, almost the same as the UIR profile. One ambiguity about the [Ne II] image is that at 12.8 μm, the image may have a contribution from the 11–13 μm emission plateau, which is not subtracted out by the 13.2 μm continuum image. This would have the most effect in the E-W profile, since it passes through a minimum of the [Ne II] emission. The broadening of the profile in this direction therefore may be related to this effect.

Both the source profiles and color map comparisons show that the UIR feature emission is slightly more extended than that mid-IR continuum emission. The similarity between the 13.2 and the 10.0 μm image profiles confirms that the distribution of the continuum emission is accurately measured, and the fact that the 11.2 μm feature image is more extended than both

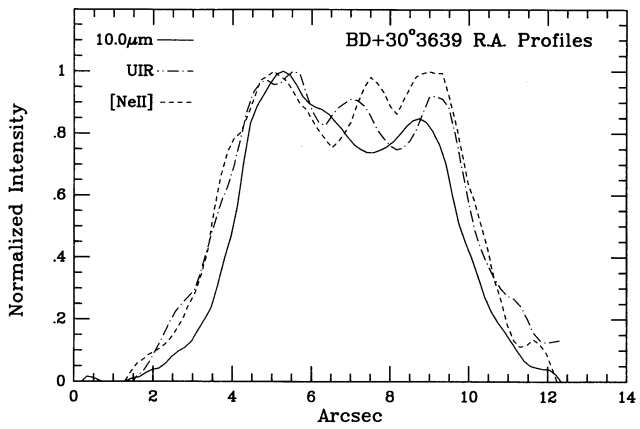

FIG. 4a

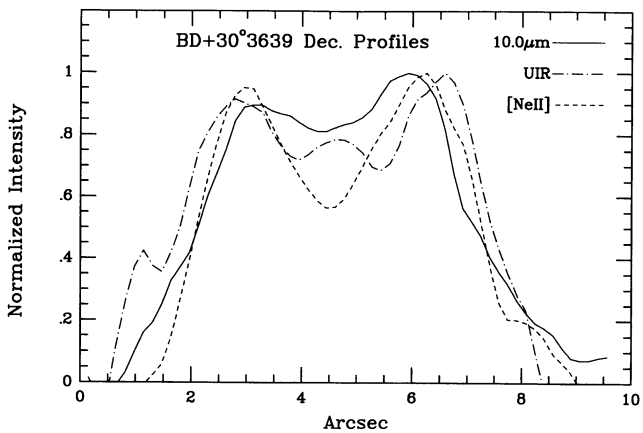

FIG. 4b

FIG. 4.—Profiles of BD +30°3639 in the [Ne II] and UIR feature images of Figs. 2c and 2e, along with the continuum profile of the 10.0 μm image of Fig. 1. These profiles have been aligned to the center position of the nebula. (a) Profiles in right ascension, with east at the left. Profiles have been normalized to the eastern peak. The UIR and [Ne II] profiles are wider than the continuum profile at 10.0 μm, both in FWHM and peak separation. (b) Profiles in declination, with south at the left. Profiles have been normalized to the north peak. Here again the UIR feature profile is wider than the 10.0 μm continuum profile. However, the [Ne II] profile is only slightly wider than the continuum.

the 13.2 and 10.0 μm images indicates that the larger extent is not a thermal effect. The comparison between the continuum and 12.8 μm images shows that the [Ne II] emission is predominantly from the N and S lobes of the nebula, whereas the continuum flux has a strong component in the E lobe.

3.3.2. *The* [Ne II] *Emission in BD +30°3639*

The [Ne II] image shows a strong similarity to the distribution of the 6 cm continuum emission from the nebula, as seen in the VLA images by Masson (1989). The [Ne II] emission, as a tracer of the ionized gas distribution, confirms the peaks of emission in the northern and southern regions as shown by the radio images. Comparison of the 12.8 μm image with the continuum and UIR feature image at 11.2 shows that the distribution of [Ne II] emission is similar to the dust emission, but the enhancements of emission in the eastern and western regions of the dust images are not present in the [Ne II] image.

Roche (1989) presents two near-IR images of BD +30°3639 at 2.166 μm (Brγ) and 3.28 μm (the position of the UIR feature). The image at Brγ is very similar to the *K* image of BD +30°3639 presented here, showing peaks to the north and south of the central star. Roche's image at 3.28 μm, however, is different from the *K* and Brγ images, showing an enhancement in the NE part of the emission ring. This is where an enhancement of the emission also appears in the 11.2 μm feature map. The similarity between the images suggests that the 3.28 and 11.2 μm features have the same spatial distribution and provides additional evidence that the UIR emission originates from a single population of grains.

TABLE 2

SIZES OF BD +30°3639

WAVELENGTH (μm)	FWHM SIZE (E-W)	FWHM SIZE (N-S)	SEPARATION OF PEAKS (E-W)	SEPARATION OF PEAKS (S-N)
2.2	5″6	5″2	3″6	3″4
10.0	5.7	5.1	3.5	2.6
11.2	6.2	5.4	3.8	3.0
12.4	6.2	4.7	3.6	2.8
12.8	6.1	5.0	3.8	2.8
13.2	5.9	5.0	3.3	2.8
UIR[a]	6.5	5.6	3.6	3.8
[Ne II][b]	6.8	5.2	4.0	3.3

[a] Calculated by subtracting a scaled 10.0 μm image from the 11.2 μm image.
[b] Calculated by subtracting a scaled 13.2 μm image from the 12.8 μm image.

3.3.3. *BD +30°3639 Color Temperature, Optical Depth Images*

A temperature image for the nebula can be calculated from the 10.0 and 13.2 μm continuum images. For grains with a power law emissivity $Q_\lambda \propto \lambda^{-n}$, the temperature is related to the intensity at each continuum wavelength $I_{10.0\,\mu m}$ and $I_{13.2\,\mu m}$ by the following equation:

$$\frac{I_{13.2\,\mu m}}{I_{10.0\,\mu m}} = \frac{Q_{13.2\,\mu m} B_{13.2\,\mu m}(T)}{Q_{10.0\,\mu m} B_{10.0\,\mu m}(T)} . \quad (1)$$

The calculation was performed for those regions where the S/N was greater than 10 in both images. Without any knowledge of the composition of the grains, the emissivity exponent *n* was taken to be 2, consistent with graphic grains (Dwek et al. 1980). The result of the calculation is shown in Figure 2. The points of highest temperature are on the ring of emission, in the E and W positions. The minimum is located at the position of the southern lobe. The temperatures in the region calculated range from approximately 160 K to 190 K, with an average temperature over the region of 172 K ± 10 K. This agrees with the value calculated based on the *IRAS* low-resolution spectrometer (LRS) data from Pottasch et al. (1986), assuming the same emissivity law. It is also interesting to note that the highest temperature region is in the eastern lobe of the nebula, farther from the central star than the N and S regions of the ring. The eastern lobe is where the UIR emission is most extended compared to the continuum flux, as shown in Figure 3b. If the emitting grains in BD +30°3639 have a different power-law emissivity exponent, the derived temperature will be higher or lower, but the location of the warmer and cooler regions of the nebula would be similar to the calculated image in Figure 2.

From the observed intensity and calculated temperature images, the opacity distribution of the dust can be determined. Assuming that the radiation from the nebula at a particular frequency I_ν is from dust grains at a temperature *T* emitting a blackbody spectrum $B_\nu(T)$, and that the temperature *T* accurately represents these grains, the following transfer equation can be solved:

$$I_\nu = (1 - e^{-\tau_\nu^{warm}}) B_\nu(T) e^{-\tau_\nu^{cold}} , \quad (2)$$

where τ_ν^{cold} is the absorption optical depth of dust between the nebula and the observer, and τ_ν^{warm} is the optical depth of the emitting grains in the nebula. Figure 2 shows a mid-IR optical depth image of BD +30°3639 where the quantity τ_ν^{warm} was calculated from the 10.0 μm image and the temperature image from Figure 2 for all points where the temperature is defined. As noted previously, without information on the composition and properties of the emitting grains, the temperature image may not represent the physical temperatures in the nebula, so the calculated image would then indicate the relative density distribution rather than the true optical depth. The quantity τ_ν^{cold} was assumed to be zero. The optical depth image in Figure 2 shows that the 10 μm emission is optically thin everywhere in the nebula, with an average opacity of $6.3 \times 10^{-4} \pm 1.3 \times 10^{-4}$. There are density enhancements along the ring of the nebula, with the most dense regions in the north and south positions. Instead of a central minimum, there is a density band that connects the N and S lobes. This image is consistent with a more dense equatorial region along the N-S axis of the nebula, as indicated by the radio continuum images, and less dense but warmer regions in the E and W poles of the nebula.

4. IC 418

The PN IC 418 is a young, low-excitation, elliptically shaped nebula with bipolar symmetry (see the images in Balick 1987 and Louise et al. 1987). This bright shell is enveloped in a much larger faint halo. A good review of the observed characteristics of IC 418 is given by Hoare (1990). The IR emission from IC 418 shows several distinct components. The near-IR emission shows an excess above what is expected from the nebular gas and the star itself (Willner, Becklin, & Visvanathan 1972). A second component in the near- and mid-IR is the UIR features, seen at 3.3, 3.4 (Russell et al. 1977), 6.2, 7.7 (Cohen et al. 1986), and possibly 11.2 μm (Willner et al. 1979). There is a broad feature at 11.3 μm which is attributed to SiC emission (Willner et al. 1979), and a strong [N II] feature at 12.8 μm. In addition, there is a broad feature which peaks near 30 μm (Moseley 1980; Forrest, Houck, & McCarthy 1981) which has been attributed to magnesium sulfide by Goebel & Moseley (1985). There is also another continuum emission component in the mid- and far-IR, which is assumed to be due to carbon grains that are larger than those responsible for the near-IR emission (Hoare 1990). Phillips, Sanchez Magro, & Martinez Roger (1984) scanned across the nebula in right ascension using a photometer with a 5".4 beam to measure the profile of IC 418, and found the nebular size increased with wavelength and was larger than their standard star profile at *H*, *K*, and *L*. Meixner et al. (1992) has imaged the nebula at several mid-IR wavelengths, including the SiC and [Ne II] emission features at 11.3 and 12.8 μm.

4.1. *IC 418 Observations*

The details of the IC 418 observations are given in Table 1. The flux standards used were HD 203856, HD 22686, and HD 40335 for the near-IR images (Elias et al. 1982) and α Tau for the images at 9.8 and 11.7 μm. As with the BD +30°3639 data, the resolution is the FWHM of the standard star images taken immediately before and after the observations of the nebula. Calibrated contour images of IC 418 at *J*, *H*, *K*, 9.8 μm and 11.7 μm are shown in Figure 5. The general features of the nebula are the same in each of the near-IR images: the overall shape of the nebula is ellipsoidal, with emission lobes on either side of the central star.

4.2. *IC 418 Morphology and Source Sizes*

There are important similarities between the NIR images presented here and the images at optical wavelengths in Louise et al. (1987). In their Hβ image, there are two main lobes of emission. A line drawn between these lobes passing through the center of the nebula has a position angle (PA) of 68°, similar to the PA for the *H* and *K* images of 70° and 76°, respectively. The separation of the peaks of the lobes is 8".8, close to that observed in the *J* image. The [O II] image by Louise et al. shows a similar double-lobed structure, with the peaks of emission at approximately the same location and separation.

Despite the similarity between the near-IR images, however, significant differences are seen. The largest differences are between the *J* image and the *H* and *K* images. One difference is that the brightest lobe of emission from the nebula in *J* is rotated approximately 45° from the position of the brightest lobe in the *H* and *K* images, at a PA of 25°. In addition to the rotation, the E lobe in the *J* image also appears to be located slightly closer to the center of the nebula, compared to the *H* and *K* images. Another difference is in the local minimum in the ring structure in the northwest part of the *H*, *K*, and optical images. The minimum is absent in the *J* image—the ring structure extends through this region without any break. The smaller west emission lobe also differs in the *J* image. Instead of a discrete local maxima, the intensity varies smoothly from the northern part of the nebula along the west side to the southern part, where there is a local minimum common to all the images.

These differences can also be seen in the source profiles. Figure 6 shows the profiles for each of the images, normalized to the level of the brightest (E) lobe of emission and centered on the central star. The profiles are at a PA of 70°, and averaged over a width (perpendicular to the direction of the profile) of 0".56. The spatial extent of the near-IR emission is different in each of the bands, with a trend of larger source extension with increasing wavelength for the NIR images. Table 3 gives the size of IC 418 at each wavelength as measured from these profiles through the main lobes.

The *J*-band emission is dominated by the 1.083 μm He I line with some contribution from Paβ (Scrimger 1984), with little excess emission, and the *H* and *K* bands contain primarily line emission from the hydrogen Brackett series with an increasingly higher IR excess, presumably due to continuum emission (Zhang & Kwok 1992). The spatial extent of the image at *J* is similar to the optical images of Louise et al., consistent with the fact that the flux is dominated by line emission. The larger spatial extent of the *H* and *K* images suggests that a significant amount of the near-IR excess emission is located near the outer edge of the ionized zone. Also, the difference in location between the *J* and the *H* and *K* lobe peaks may be an effect of the IR excess, or may be due to the different distribution of

TABLE 3

OBSERVED PARAMETERS OF IC 418

Filter	FWHM Size	Nebular Peak Separation
J	11".3	8".6
H	12.3	9.2
K	12.5	9.8
9.8 μm	11.7	...
11.7 μm	11.5	...

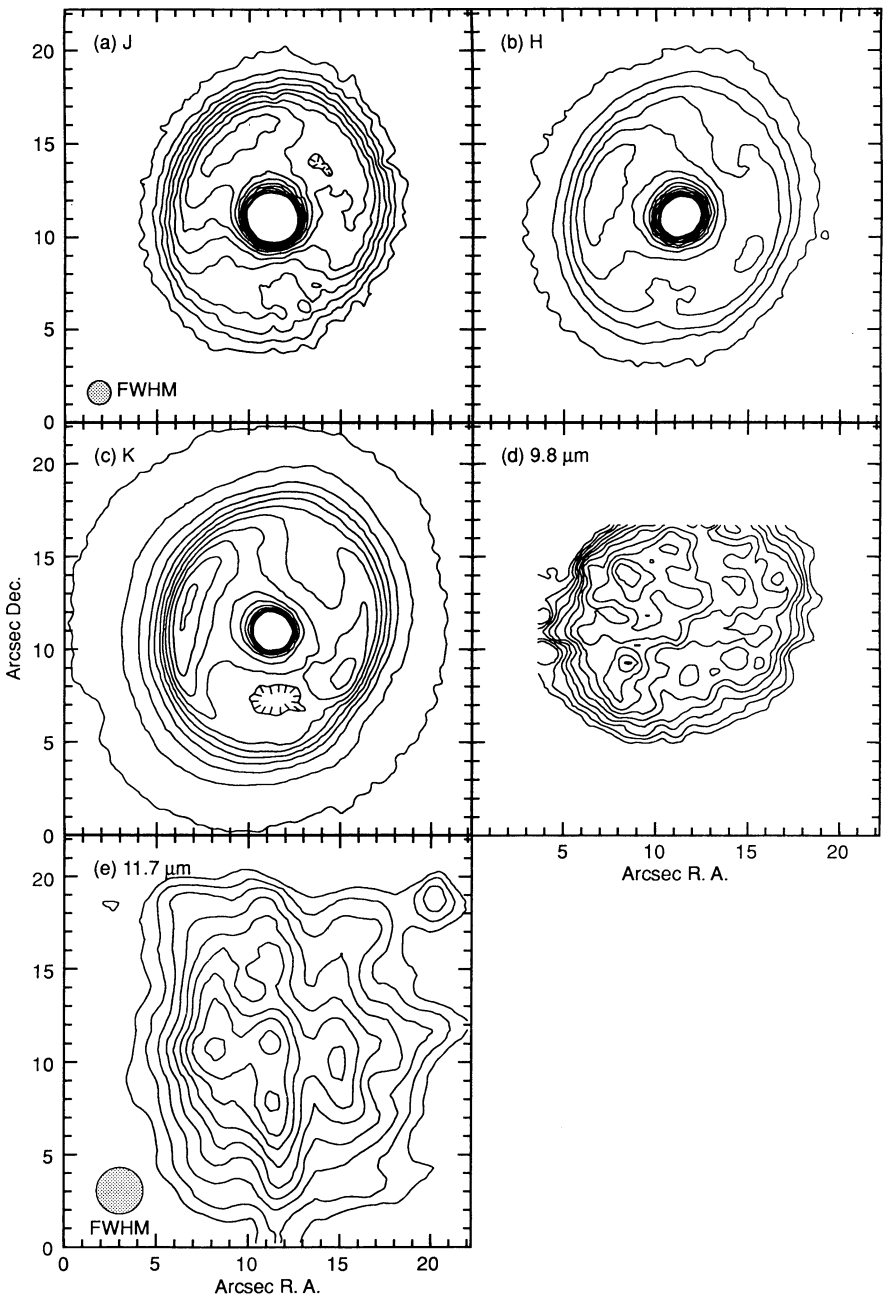

FIG. 5.—Calibrated contour images of IC 418 at *J*, *H*, *K*, 9.8 μm, and 11.7 μm. The contour spacing has been chosen to display the nebular structure, so the levels cut off before the peak of the central star is reached. In every case the minimum contour level is $>5\,\sigma$ above the background noise level. The position angle (PA) of the lobes given for each image is the angle E of N of a line drawn through the peak of the lobes, passing through the center of the nebula. (*a*) *J* image: contour spacing 0.75 mJy arcsec^{-2}, lowest level 0.75 mJy arcsec^{-2}. Lobe PA = 25°. The circle shown is the FWHM size of the standard star at *J* (1.″3), typical for the NIR images (see Table 1). (*b*) *H* image: contour spacing 0.75 mJy arcsec^{-2}, lowest level 0.75 mJy arcsec^{-2}. Lobe PA = 70°. (*c*) *K* image: contour level spacing 0.75 mJy arcsec^{-2}, lowest level 0.75 mJy arcsec^{-2}. Lobe PA = 76°. (*d*) 9.8 μm image: contour level spacing 32 mJy arcsec^{-2}, minimum level 64 mJy. Lobe PA = 70°. (*e*) 11.7 μm: contour spacing 140 mJy arcsec^{-2}, starting at 100 mJy arcsec^{-2}. Lobe PA = 56°. The circle shown is the FWHM size of the standard star for this wavelength (2.″5).

emission from the 1.083 μm He I line and the hydrogen Brackett lines.

4.3. *IC 418 Central Star Subtraction*

To study the PN, it would be useful to separate out the central star emission from the nebular flux. We obtained images of nearby SAO catalog stars to determine the instrumental PSF at the time of the PN observations. The flux contribution from the central star can be removed from the nebular image by subtracting a scaled reference star image. When this is done for the images of IC 418 at *J*, *H*, and *K*, the central peak of the nebula is broader than the standard star image, so the central peak cannot be totally accounted for by emission from the central star. The reference star was scaled to be the maximum value possible that would not create a local minimum in the central peak of the PN, as shown in Figure 7. The results of the subtraction are illustrated in Figure 8. For each wavelength, the original profile, the profile of the star, and

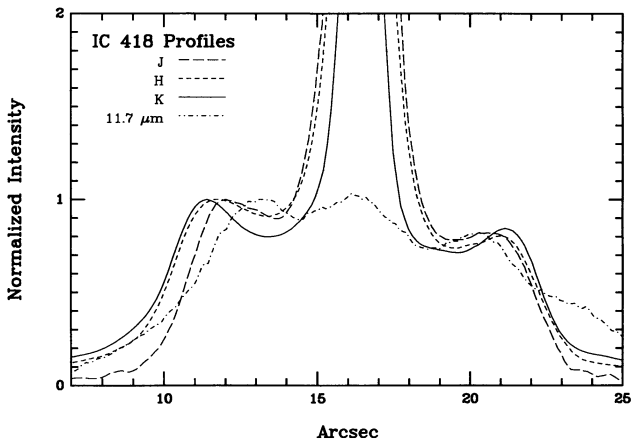

FIG. 6.—Profiles of IC 418 through the major lobes (PA = 70°). The profiles have been normalized so that the NE lobe peak is 1.0, and the profiles aligned to the central star. Each wavelength is assigned a different line type, shown below the figure. The *K* image profile has the largest spatial extent, followed by the *H*, *J*, and 11.7 μm image profiles.

the result after subtraction is shown. The residual central peak in the *J* image has the highest intensity relative to the rest of the nebula, and decreases as a function of wavelength at *H* and *K*. Table 4 gives the near-IR fluxes of IC 418 at each wavelength for each of the components of IC 418. Note that the flux given for the star is an upper limit: there may be unresolved emission from the region near the central star that is included in this value.

It is possible that the excess emission near the central star in these images could be artificially created by the instrument or data reduction process. For example, if the instrumental PSF in the images of the nebula were vastly different from that in the standard star observations, the star would be subtracted

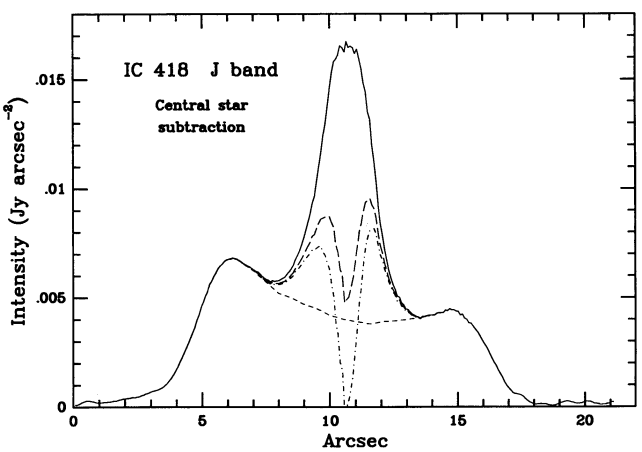

FIG. 7.—Profiles of IC 418 at *J*, showing the central star subtraction process. The solid line shows the original data profile. When the central star is scaled to the level expected from the outer nebular shell (*short dashed line*), Two residual peaks are left (*long dash line*), corresponding to a ring around the central position. Even if the star is scaled to subtract all of the flux at the central separation position (as in the dot-dash profile), residuals still remain on either side of the central position. These residual feature are narrower than the instrumental PSF, so we assume that it is more likely that there is another spatially extended emission component in the central region. The unresolved central star flux is taken to be the maximum possible value that does not create a central minimum as in the long-dash profile. This method was used for the images shown in Fig. 8.

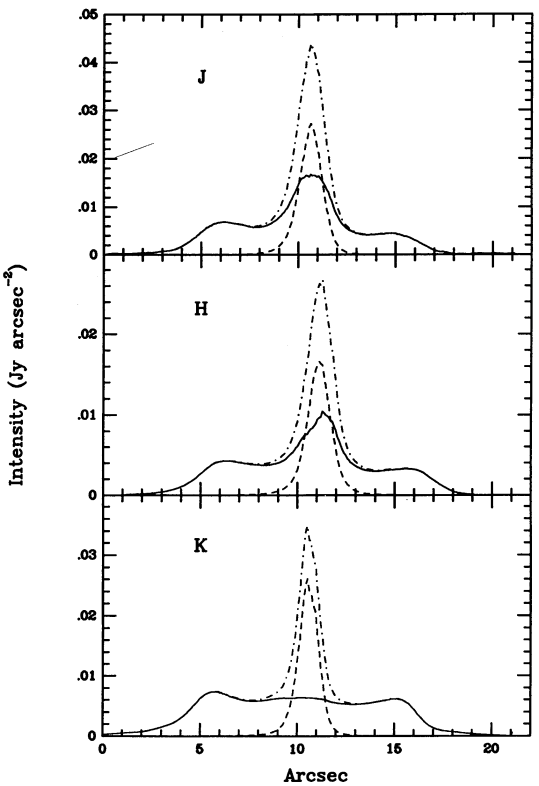

FIG. 8.—PSF-subtracted profiles of IC 418 at *J*, *H*, and *K*. These profiles show the original data (*dot-dash line*), the scaled standard star (*dashed line*), and the resulting profile when the star is subtracted (*solid line*).

improperly. However, several steps were taken to make sure the standard star images were taken under the same conditions as the images of the nebula The images of the PSF standard stars were taken immediately before and after the observations of the nebula at each wavelength. The integration times and number of observations per source were similar for both the standard stars and the nebula. The stars used (SAO 150440 and SAO 150445) were not excessively bright and the integration times were short enough to prevent saturation, so there is no reason to expect a flux-dependent PSF difference between the stars and the nebula. The stars are only a few arcminutes away from IC 418, so the observations were obtained in the same region of the sky. When comparing the standard star images taken before and after the images of the nebula at a particular wavelength, there was no significant difference in the source profiles. This indicated that the conditions were stable throughout the observations at a particular wavelength. We therefore have some confidence that the central excess is real and not an artifact of the data-taking process. A simple model of the emission is unresolved emission from the central star

TABLE 4

IC 418 COMPONENT FLUXES (Jy)

Filter	Total	Nebula	Star	Central Excess	Halo
J.....	0.823	0.655	0.086	0.082	<0.038
H.....	0.732	0.524	0.064	0.032	0.112
K.....	1.24	0.938	0.073	0.011	0.218

(represented by the scaled PSF profile in Fig. 8) plus an extended emission component shown by the residual profile in Figure 8.

4.4. *Sources of Near-IR Emission in IC 418*

There are several components in the near-IR emission from IC 418. One of these is the component due to recombination emission from the nebula. The total nebular flux between 2 and 4 μm is a factor of 2 greater than what is expected from the radio observations (Willner et al. 1979), implying the presence of hot dust. Willner et al. calculated a grain temperature of 1350 K for a 10″ beam, and 950 K for a 44″ beam, assuming a grain emissivity $Q_\lambda \propto \lambda^{-2}$. However, they find it difficult to explain these high temperatures given the central star temperature of $\sim$30,000 K. Other mechanisms, such as free-free emission generated from interactions between electrons and H^- or H_2^- ions, or stellar radiation scattered from dust particles, are also not satisfactory to explain the excess. Emission from H_2 is not expected from within the ionized region, and has not been detected at 2.121 μm in spectra of the nebula (Hora 1993).

Recently, Zhang & Kwok (1992) measured the spectrum of IC 418 between 1.5 and 1.75 μm (the *H* band) with a spectral resolution of $\lambda/\Delta\lambda = 1280$. The main features of the spectrum in the wavelength region from 1.5 to 1.75 μm are the series of Brackett emission lines of hydrogen superimposed on a continuum. There is an uncertainty in the measured flux from the nebula since the instrumental beam diameter was only 5″, significantly smaller than the size of the nebula. Zhang & Kwok multiply the entire spectrum by a factor of 5 to correct for the small beam size. However, since most of the nebula flux originates from a radius larger than 5″ radius, and the nebular shape is seen to differ as a function of wavelength, the small beam could cause differences in the spectral shape as a function of position over the nebula.

From their observations, Zhang & Kwok determined the *H*-band excess and estimated the excess at *J* and *K* after correcting for line emission. The excess emission at *K* and *L* is consistent with a blackbody temperature of 1350 K, but it does not explain the continuum in the *H*-band spectrum which rises sharply toward shorter wavelength. They attribute the hot (1350 K) dust component to nonequilibrium heating of small grains (Sellgren 1984) and suggest the possibility of another continuum emission component that peaks between 1.25 and 1.65 μm to explain the *H*-band continuum. The images of IC 418 and the profiles presented in Figure 8 show that there is a strong central excess at *J* and *H*, with little emission in the *K*-band. This excess may be related to the hotter component seen in Zhang & Kwok's *H*-band spectrum. The central location of this excess is consistent with the beam position for the spectral data and is a plausible location for the high temperature emission.

4.5. *IC 418 Halo Emission*

Evidence for an extended halo of emission around IC 418 have been reported previously. Willner et al. (1972) showed that the total flux detected from the nebula continued to increase out to a beam size of 40″ at *K*. Taylor & Pottasch (1987) detected neutral hydrogen in the circumnebular shell. Their observations showed 21 cm emission and absorption toward the nebula, with a velocity relative to the system of 13.2 ± 0.5 km s^{-1}. Taylor, Gussie, & Goss (1989) mapped the 21 cm emission and found it to be extended by approximately 1′ in right ascension and 2′ in decl. Monk, Barlow, & Clegg (1989) detected a faint halo in [O II] and Hγ extending at least 110″ in diameter. They attributed the emission to scattered light from small ($<$0.03 μm for carbon or silicate) particles. Phillips, Riera, & Mampaso (1990) mapped the envelope in H I + [N II] and also saw evidence for emission at *H* and *K* beyond the H II zone.

We have shown in the source profiles in Figure 6 that the nebula is more extended in the longer near-IR wavelengths, based on the profile FWHM and separation of the lobe peaks. There is also evidence in these profiles for a low level emission from the nebula in the *H* and *K* images that extends well outside the ionized zone (as defined by the emission line profiles by Louise et al. 1987) where most of the flux is emitted. Figure 9 shows the profiles of the images plotted again on a magnified vertical scale. This shows the emission from the *H* and *K* bands extending out beyond the bright lobe of the nebula, to approximately 14″ from the lobe peak. In contrast, the *J* emission terminates shortly after the major lobe of emission in the nebula, at no more than 7″ from the lobe peak. The *K* emission is brighter than the *H* emission, relative to the lobes of the nebula. The *J* image has a lower signal-to-noise (S/N) ratio than the *K* and *H* images, but is clear that, relative to the lobe peak, the emission drops much lower at a given distance.

The color temperature of the emission outside the ionized zone can be calculated using the *H* and *K* images. The resulting image has a roughly flat distribution, with an average temperature of 1500 K. This is most likely not the physical temperature of emitting grains in this region, since there are mechanisms other than thermal emission that could contribute to the IR flux from this region. If there is a significant contribution from scattered light in the halo, the relative contribution will be greater at *H*, so the temperature would be lower. Spatially resolved polarization images of IC 418 would help distinguish between thermal emission and scattered light in the nebula. The halo emission may also be due to nonequilibrium heating of small grains (e.g., Sellgren 1984). The roughly constant color temperature of the detected halo region is consistent with this model. Deep narrow-band imaging of the halo

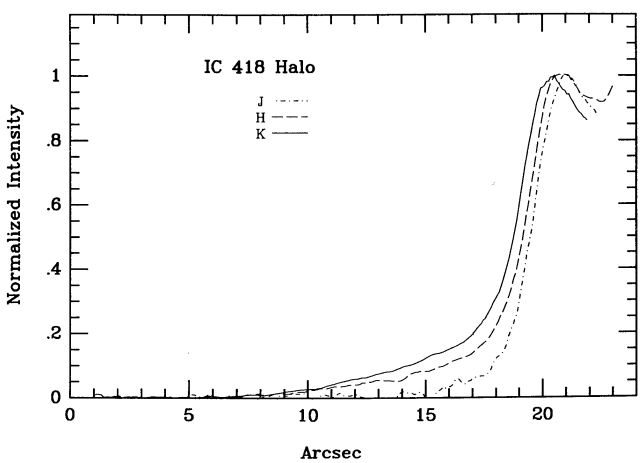

FIG. 9.—Profiles of IC 418, in the same direction as previous profiles, extending further to the NE and including the NE lobe peak. The profiles have been aligned on the central star, and the profiles have been scaled to match the peak lobe intensity. The profiles show the halo emission in *H* and *K*, and the much weaker emission in the *J* profile beyond the nebular shell.

region would determine if the halo emission is from scattered line flux from the ionized region, or continuum emission from transitory heating of small grains.

4.6. *IC 418 Mid-IR Emission*

The contour images of IC 418 at 9.8 and 11.7 μm are shown in Figure 5. The 11.7 μm filter samples the emission feature in the spectrum of IC 418 from 11 to 12.5 μm which is attributed to SiC. Evidence of weak UIR emission at 3.3 and 7.7 μm has been detected (Willner et al. 1979), so there may be some weak contribution from the UIR feature at 11.2 μm, as well as from the UIR plateau feature. No silicate emission feature is apparent in the mid-IR spectrum. There is also a large contribution at 11.7 μm from mid-IR continuum emission from the nebula. The relative importance of these contributions to the total emission is not precisely known.

The image of IC 418 at 9.8 μm is markedly different from the near-IR and optical images of the nebula. The outer oval shape is similar, but the majority of the flux is coming from the NE of the nebula. There is no corresponding peak in the SW region, as in the other images. The size of the emitting region, however, is similar to the near-IR and optical images. The FWHM sizes of IC 418 are compared in Table 4. The 11.7 μm image of IC 418 is more difficult to compare in detail to the other images because of its lower spatial resolution. Meixner et al. (1992) have obtained an image of IC 418 at 11.3 μm at a higher spatial resolution that shows an ellipsoidal shape similar to our 9.8 μm image. One feature that is readily visible in the images of the SiC emission feature is the central at the location of the central star. The central peak is not seen in the 9.8 μm image. No significant flux is expected from the central star or ionized gas at this wavelength, and it is not due to the continuum dust emission as evidenced by the 9.8 μm image, so the central emission is possibly due to the 11.3 μm SiC feature emission. The central peak may be related to the excess near-IR emission seen in the same spatial location in the nebula.

SiC has been thought to form in carbon star envelopes (Treffers & Cohen 1974; Merrill & Stein 1976). The envelopes of these stars have the conditions necessary for particles to form: high densities ($\geq 10^9$ cm^{-3}) and cool temperatures (1000-2000 K) (Salpeter 1974; Seab 1988). Experimental results by Frenklach, Carmer, & Feigelson (1989) have shown that SiC can form at higher temperatures (above 2800 K) and therefore would be the first particles to form in C-rich envelopes. They have proposed that SiC may act as nucleation sites for larger carbon particles and formation of PAH molecules. The observations at 11.7 μm presented here are consistent with this model of SiC formation and growth. Since the carbon abundance is not very high (C/O ratio ≈ 1.3) the carbon is locked up in CO and SiC, leaving little carbon for the formation of amorphous grains or PAHs. The UIR emission from IC 418 is in fact much weaker than in other IR-bright nebula, as shown by Cohen et al. (1986) who compared the 7.7 μm feature flux to total far-IR luminosity. The spatial distribution of the 11.7 μm emission also indicates that it is different from the UIR features that exist near the outer edge of the ionized zone (e.g., in NGC 7027 or BD +30°3639).

The IR spectrum of IC 418 beyond 10 μm consists of a thermal continuum with an emission feature near 30 μm attributed to MgS (Willner et al. 1979). Models of the SiC emission have shown that it cannot account for the far-IR emission by two to three orders of magnitude (Stephens 1980; Hoare 1990).

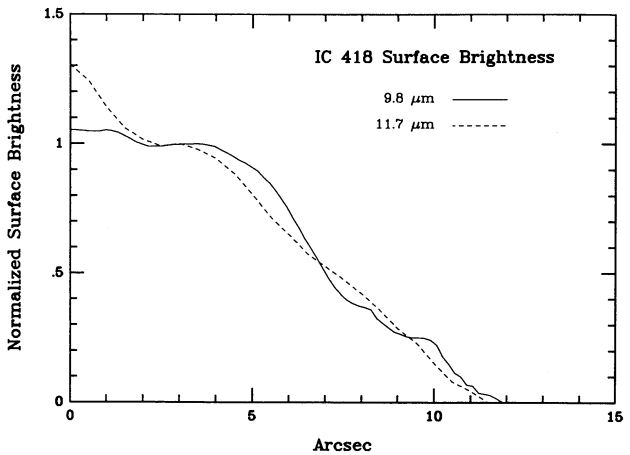

FIG. 10.—Observed surface brightness of IC 418 at 9.8 (*dotted line*) and 11.7 μm (*dashed line*), determined from the images in Fig. 5. The surface brightness in Jy arcsec^{-2} is plotted as a function of distance from the center of the nebula in arcseconds.

Hoare presents two different models for the mid- and far-IR emission. Both use SiC and MgS to create the spectral features at around 11.3 and 30 μm, and the continuum is produced by graphite emission in one model and amorphous carbon in the other. The amorphous carbon model fits the *IRAS* data slightly better than the graphite model; however, both models have difficulty reproducing the near- and mid-IR continuum emission, where hot dust and UIR features will have a contribution. The surface brightness as a function of angular radius from the center of the nebula is shown in Figure 10 for the 9.8 and 11.7 μm images. This can be compared to the 12 μm model surface brightness in Hoare (1990). The actual surface brightness at 9.8 μm lacks the central peak of the 11.7 μm image and Hoare's model and is dominated at 5″ by the bright NE lobe. The differences between the mid-IR images suggests that the spatial distribution of the thermal dust and SiC is different within the nebula.

5. UIR EMISSION IN PNs

Lenzuni, Natta, & Panagia (1989) have classified 80 PNs into three groups, based on the observed C/O ratio and the presence of the 9.8 μm silicate feature and the 11.3 μm silicon carbide feature. PNs with C/O > 1.8 (such as BD +30°3639) are termed carbon-rich (C2), PNs with a silicon carbide feature and 0.85 < C/O < 1.7 (such as IC 418) are moderately carbon rich (C1), and PNs with C/O < 0.8 are oxygen-rich (O). Included in the C2 category is the well-studied nebula NGC 7027, and included in C1 is the nebula NGC 6572.

The UIR emission features in the near- and mid-IR often show differences in their spatial distribution when compared to the continuum emission. This has been demonstrated before for other PNs in group C2. In NGC 7027, Woodward et al. (1989) concluded that the UIR feature emission at 3.28 and 3.4 μm is spatially distinct from the continuum emission, being slightly more extended. The UIR emission was also determined to extend beyond the ionized region of the nebula, as defined by the Br α flux at 4.052 μm. The same was concluded for the mid-IR UIR emission (Aitken & Roche 1983; Arens et al. 1984). Cohen et al. (1986) has shown a correlation between the UIR emission strength and the C/O ratio, pointing to a carbonaceous origin for the UIR features. In BD +30°3639, there

is evidence of the 3.28 μm UIR feature being spatially distinct from the ionized zone, as defined by the Brγ emission (Roche 1989). The UIR features at 7.7, 8.6, and 11.2 μm have also been found to be distinct from the dust continuum and ionized regions of the nebula (Bentley et al. 1984); Hora et al. 1990; this work). The distribution of the UIR emission is similar in the different UIR features at 3.3, 7.7, and 11.2 μm, being in general more extended than the continuum and ionized regions.

The PNs in the group C1 also show spatial variations of the components of IR emission. In NGC 6572 there exists distinct variations in its mid-IR flux as a function of wavelength, with evidence for extended emission in the UIR feature at 11.2 μm (Hora et al. 1990; Deutsch 1990). The PNs IC 418 and NGC 6572 both exhibit the feature at 11.3 μm attributed to SiC emission. IC 418 is unique in that some emission from this feature seems to originate from the center of the nebula.

The spatially resolved observations of the IR emission support a model where the carriers of the UIR features are different from the source of the continuum dust emission. In the nebulae studied here, the UIR emission is more extended than the continuum dust emission, although it is certainly overlapping the ionized zone and may be present within it. The fact that the emission is more extended may be a result of destruction of the UIR carriers on the interior edge of the shell from absorption of strong UV flux from the central star. All the characteristics described above are consistent with the UIR emission being from a mixture of PAH molecules. They have characteristic bands in each of the UIR feature emission regions, and although no one PAH has been observed to match the spectrum of an astronomical source, the most likely case is that a mixture of PAHs, at various temperatures, molecule sizes, and states of hydrogenation are responsible for the emission in each object. Frenklach & Feigelson (1989) have shown in modeling the conditions in carbon-rich circumstellar envelopes that PAH molecules can form under the expected conditions. The PAH molecules will be susceptible to dissociation by absorption of UV photons (Duley 1987), with smaller molecules being easiest to dissociate. This may explain why the UIR emission is located on the outer edge of PNs—they may be destroyed by UV flux on the inner side of the PN shell. There is other evidence of an anticorrelation of UIR emission to objects with high UV flux (Roche 1987; Puget & Léger 1989).

6. CONCLUSIONS

Images of the PN BD +30°3639 and IC 418 have been presented at several IR wavelengths which show the spatial distribution of each of the spectral components in the nebulae. In BD +30°3639, the UIR emission at 11.2 μm is emitted primarily from the outer rim of the nebula, as defined by the mid-IR continuum emission. The UIR plateau emission at 12.4 μm is seen to have a different spatial distribution than the 11.2 μm UIR feature, suggesting that the mechanisms or conditions necessary to excite the plateau emission may be different than for the 11.2 μm feature. The calculated temperature image for BD +30°3639 shows that the average nebular temperature is 172 K, with the highest temperature regions in the E and W parts of the ring of the nebula. The opacity image shows the emission to be optically thin throughout the nebula, with opacity maxima in the northern and southern regions of the ring. The distribution of 12.8 μm [Ne II] feature emission in BD +30°3639 and the near-IR image which is dominated by recombination emission are morphologically similar to published radio continuum images of the nebula, confirming that the ionized gas emission peaks are in the N and S lobes. The mid-IR continuum emission differs in that there is an additional peak in the E lobe of the nebula, which is a region of higher dust temperature.

The distribution of emission in IC 418 seen in the near-IR images is consistent with a small contribution from thermal emission by dust grains on the outer edge of the nebula. There is also a central excess in the flux distribution of the near-IR IC 418 images after subtracting out the contribution from the central star. The residual excess is strongest at *J* and is progressively weaker at *H* and *K*. This excess at the central position indicates a possible compact shell interior to the main shell of emission. The central peak seen in the 11.7 μm image suggests the presence of SiC near the central star. An extended halo is seen in the *K* and *H* images which extends approximately 13″ farther than the peaks of the main lobes, for a total nebular diameter of 36″ along the minor axis and 40″ along the major axis of the nebula. Halo emission is not detected in the *J* band or the mid-IR images. The halo may include contributions from scattered light from the central star and nebula, and non-equilibrium heating of small grains in the halo.

The MIRAC project has received support from National Science Foundation grant AST-8820904, Naval Research Laboratory, Smithsonian Astrophysical Observatory (Smithsonian Institution Scholarly Studies grants 1240S821 and 1240S921), Steward Observatory, and USAF Phillips Laboratory. We thank G. Albright and S. Augustine of Hughes Aircraft Co. for their assistance during the MIRAC design phase and the initial operation of the detector array.

REFERENCES

Aitken, D. K., & Roche, P. F. 1982, MNRAS, 200, 217
———. 1983, MNRAS, 202, 1233
Arens, J. F., Lamb, G. M., Peck, M. C., Moseley, H., Hoffmann, W. F., Tresch-Fienberg, R. M., & Fazio, G. G. 1984, ApJ, 279, 685
Balick, B. 1987, AJ, 94, 671
Ball, R., Arens, J. F., Jernigan, G., & Keto, E. 1991, in Astrophysics with Infrared Arrays, ed. R. Elston (ASP Conf. Ser., 14), 171
Basart, J. P., & Daub, C. T. 1987, ApJ, 317, 412
Bentley, A. F., Hackwell, J. A., Grasdalen, G. L., & Gehrz, R. D. 1984, ApJ, 278, 665
Cohen, M., Allamandola, L., Tielens, A. G. G. M., Bregman, J., Simpson, J. P., Witteborn, F. C., Wooden, D., & Rank, D. 1986, ApJ, 302, 737
Deutsch, L. K. 1990, Ph.D. thesis, Harvard Univ.
Duley, W. W. 1987, in Polycyclic Aromatic Hydrocarbons and Astrophysics, ed. A. Léger, L. d'Hendecourt, & N. Boccara (Dordrecht: Reidel), 373
Dwek, E., Sellgren, K., Soifer, B. T., & Werner, M. W. 1980, ApJ, 238, 140
Elias, J. H., Frogel, J. A., Matthews, K., & Neugebauer, G. 1982, AJ, 87, 1029
Frenklach, M., Carmer, C. S., & Feigelson, E. D. 1989, Nature, 339, 196
Frenklach, M., & Feigelson, E. D. 1989, ApJ, 341, 372
Goebel, J. H., & Moseley, H. 1985, ApJ, 290, L35
Forrest, W. J., Houck, J. R., & McCarthy, J. F. 1981, ApJ, 248, 195
Hoare, M. G. 1990, MNRAS, 244, 193
Hoffmann, W. F., Hora, J. L., Fazio, G. G., & Shivanandan, K. 1993, in preparation
Hora, J. L. 1991, Ph.D. thesis, Univ. of Arizona
———. 1993, in preparation
Hora, J. L., Deutsch, L. K., Hoffmann, W. F., & Fazio, G. G. 1990, ApJ, 353, 549
Léger, A., & Puget, J. L. 1984, A&A, 137, L5
Lenzuni, P., Natta, A., & Panagia, N. 1989, ApJ, 345, 306
Louise, R., Macron, A., Pascoli, G., & Maurice, E. 1987, A&AS, 70, 201
Masson, C. R. 1989, ApJ, 346, 243
Meixner, M., Ball, J. R., Arens, J. F., & Jernigan, J. G. 1992, in IAU Symp. 155, Planetary Nebulae, ed. R. Weinberger & A. Acker (Dordrecht: Kluwer), in press
Merrill, K. M., & Stein, W. A. 1976, PASP, 88, 285
Monk, D. J., Barlow, M. J., & Clegg, R. E. S. 1989, in IAU Symp. 131, Planetary Nebulae, ed. S. Torres-Peimbert (Dordrecht: Kluwer), 197

Moseley, H. 1980, ApJ, 238, 892
Phillips, J. P., Riera, A., & Mampaso, A. 1990, A&A, 234, 454
Phillips, J. P., Sanchez Magro, C., & Martinez Roger, C. 1984, A&A, 133, 395
Pottasch, S. R., Preite-Martinez, A., Olnon, F. M., Mo Jing-Er, & Kingma, S. 1986, A&A, 161, 363
Puget, J. L., & Léger, A. 1989, ARA&A, 27, 161
Rieke, M. J., Rieke, G. H., & Montgomery, E. F. 1987, in Infrared Astronomy with Arrays, ed. C. G. Wynn-Williams & E. E. Becklin (Honolulu: Univ. of Hawaii), 213
Roche, P. F. 1987, in Polycyclic Aromatic Hydrocarbons and Astrophysics, ed. A. Léger, L. d'Hendecourt, & N. Boccara (Dordrecht: Reidel), 307
———. 1989, in IAU Symp. 131, Planetary Nebuale, ed. S. Torres-Peimbert (Dordrecht: Kluwer), 117
Russell, R. W., Soifer, B. T., & Merrill, K. M. 1977, ApJ, 213, 66
Salpeter, E. E. 1974, ApJ, 193, 579
Scrimger, J. N. 1984, ApJ, 280, 170
Seab, C. G. 1988, in Dust in the Universe, ed. M. E. Bailey & D. A. Williams (Cambridge: Cambridge Univ. Press), 303
Selgren, K. 1984, 277, 623
Smith, M. G., Gaballe, T. R., Aspin, C., McLean, I. S., & Roche, P. F. 1989, in IAU Symp. 131, Planetary Nebulae, ed. S. Torres-Peimbert (Dordrecht: Kluwer), 178
Stephens, J. R. 1980, ApJ, 237, 450
Taylor, A. R., Gussie, G. T., & Goss, W. M. 1989, ApJ, 340, 932
Taylor, A. R., & Pottasch, S. R. 1987, A&A, 176, L5
Treffers, R., & Cohen, M. 1974, ApJ, 188, 545
Witteborn, F. C., Sanford, S. A., Bregman, J. D., Allamandola, L. J., Cohen, M., Wooden, D. H., & Graps, A. L. 1989, ApJ, 341, 270
Willner, S. P., Becklin, E. E., & Visvanathan, N. 1972, ApJ, 175, 699
Willner, S. P., Jones, B., Puetter, R. C., Russell, R. W., & Soifer, B. T. 1979, ApJ, 234, 496
Woodward, C. E., Pipher, J. L., Shure, M., Forrest, W. J., & Sellgren, K. 1989, ApJ, 342, 860
Woolf, N. J. 1969, ApJ, 157, L37
Zhang, C. Y., & Kwok, S. 1992, ApJ, 385, 255